



Valproate-coenzyme A conjugate blocks opening of receptor binding domains in the spike trimer of SARS-CoV-2 through an allosteric mechanism

Federica Maschietto ^{a,1,2}, Tianyin Qiu ^{a,1,3}, Jimin Wang ^{b,*,1,4}, Yuanjun Shi ^{a,5}, Brandon Allen ^{a,6}, George P. Lisi ^{c,7}, Elias Lolis ^{d,8}, Victor S. Batista ^{a,*,9}

^a Department of Chemistry, Yale University, New Haven, CT 06520-8449, USA

^b Department of Molecular Biophysics and Biochemistry, Yale University, New Haven, CT 06520-8114, USA

^c Department of Molecular and Cell Biology and Biochemistry, Brown University, Providence, RI 02912, USA

^d Department of Pharmacology, Yale University, New Haven, CT 06520-8066, USA

ARTICLE INFO

Article history:

Received 20 September 2022

Received in revised form 13 January 2023

Accepted 13 January 2023

Available online 16 January 2023

Keywords:

Valproic acid

Valproate

VPA

3-oxo-VPA

VPA-CoA

Spike protein

Loaded springs

Triggering mechanisms

Chemical knowledge-based drug design

ABSTRACT

The receptor-binding domains (RBDs) of the SARS-CoV-2 spike trimer exhibit “up” and “down” conformations often targeted by neutralizing antibodies. Only in the “up” configuration can RBDs bind to the ACE2 receptor of the host cell and initiate the process of viral multiplication. Here, we identify a lead compound (3-oxo-valproate-coenzyme A conjugate or Val-CoA) that stabilizes the spike trimer with RBDs in the down conformation. Val-CoA interacts with three R408 residues, one from each RBD, which significantly reduces the inter-subunit R408-R408 distance by ~ 13 Å and closes the central pore formed by the three RBDs. Experimental evidence is presented that R408 is part of a triggering mechanism that controls the prefusion to postfusion state transition of the spike trimer. By stabilizing the RBDs in the down configuration, this and other related compounds can likely attenuate viral transmission. The reported findings for binding of Val-CoA to the spike trimer suggest a new approach for the design of allosteric antiviral drugs that do not have to compete for specific virus-receptor interactions but instead hinder the conformational motion of viral membrane proteins essential for interaction with the host cell. Here, we introduce an approach to target the spike protein by identifying lead compounds that stabilize the RBDs in the trimeric “down” configuration. When these compounds trimerize monomeric RBD immunogens as co-immunogens, they could also induce new types of non-ACE2 blocking antibodies that prevent local cell-to-cell transmission of the virus, providing a novel approach for inhibition of SARS-CoV-2.

© 2023 The Author(s). Published by Elsevier B.V. on behalf of Research Network of Computational and Structural Biotechnology. This is an open access article under the CC BY-NC-ND license (<http://creativecommons.org/licenses/by-nc-nd/4.0/>).

1. Introduction

The mechanism of SARS-CoV-2 infection and multiplication is mediated by molecular interactions between the viral spike protein and the ACE2 receptor of the host cell. The fusion of the viral and host cellular membranes enables the virus to infect the host cell for transferring its genetic materials [1,2]. This mechanism is primarily responsible for person-to-person transmission of the virus and the long-distant cellular transmission within infected individuals. The virus hijacks the host glycosylation machinery to camouflage viral epitopes of the spike protein, excluding the receptor-binding motif (RBM, residues N437-Y508) of the receptor-binding domain (RBD, N317-N544) that is necessary for binding the ACE2 receptor [1–3]. The transmissibility of the virus via this mechanism results from a

* Corresponding authors.

E-mail addresses: jimin.wang@yale.edu (J. Wang), victor.batista@yale.edu (V.S. Batista).

¹ These authors made equal contributions to this study.

² ORCID: 0000-0002-5995-2765.

³ ORCID: 0000-0002-3490-8469.

⁴ ORCID: 0000-0002-4504-8038.

⁵ ORCID: 0000-0002-9240-6950.

⁶ ORCID: 0000-0002-5512-1892.

⁷ ORCID: 0000-0001-8878-5655.

⁸ ORCID: 0000-0002-7902-7868.

⁹ ORCID: 0000-0002-3262-1237.

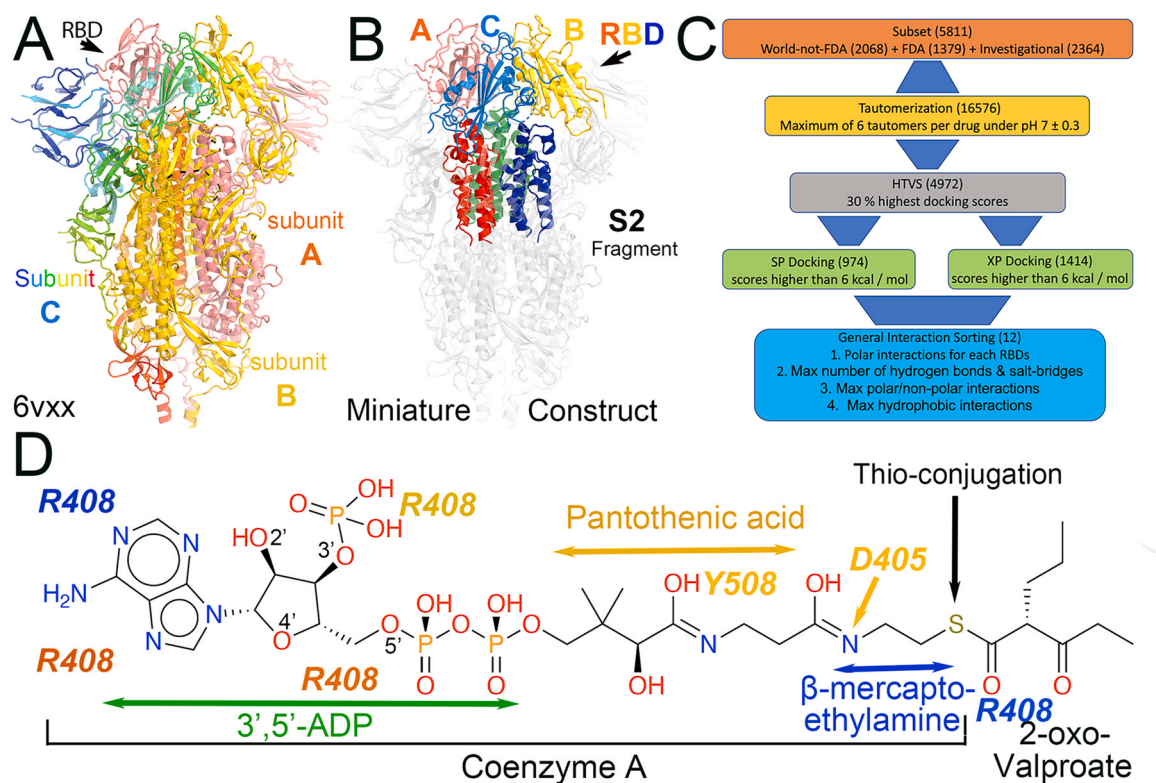


Fig. 1. Computational design for studying the initial triggering mechanism of spike RBD's trimer and the chemical structure of 2-oxo-valproate coenzyme A conjugate (VPA-CoA). (A) The spike trimer in a closed conformation (PDB/ID, 6vxx) in salmon for subunit A, gold for subunit B, and colored in rainbow scheme for subunit C. (B) A reduced model (or miniature construct) of the spike trimer contains RBD trimer with a minimal S2 fragment trimer in solid color used in this study while the omitted structures are in light gray. (C) Schematic drawing of computational procedures for identifying lead compounds starting with commercially available 5811 small molecules taken from the ZINC library through steps of tautomerization optimization, high-throughput virtual screening (HTVS), standard precision (SP) and extensive sampling precision (XS) docking, followed by selection criteria for lead compounds. (D) The chemical structure of VPA-CoA. The sites of interactions are indicated: (i) R408 from all three subunits are H-bonded to 3'-phosphate, O4'/O5' or carbonyl of valproate, (ii) two R408 stack against both sides of the adenosine ring of CoA, (iii) D405 of subunit B is H-bonded to the amide of the β-mercapto-ethylamine fragment of CoA, and (iv) Y508 of subunits B is H-bonded to the non-chiral hydroxyl or its keto form of the pantothenic acid fragment of CoA.

delicate balance between hiding the RBM epitopes for immune evasion with all three RBDs in the "down" conformation in a closed state and searching for the ACE2 receptor in a partially open configuration with one RBD in the "up" position.

In mature virions of the SARS-CoV-2 prototype at pH 7.2, 31 % of the spike trimers are in the fully closed configuration, 55 % are in the partially open state with one RBD in the up position, and 14 % are in a more open state with two RBDs in the up position, highlighting the critical role that the RBD dynamics can play in the pathogen transmissibility [4]. Many cellular factors can modulate the RBD dynamics. For example, spontaneous mutations including D614G and those of the Omicron variant can significantly alter the RBD dynamics [5], and so can the binding of many neutralizing antibodies to different parts of the spike protein [6]. At pH 4.0, the spike protein can be stabilized only in the fully closed state [7], and so would be initially released mature virions through acidified secretory pathways [8,9]. Furthermore, fatty acids are known to bind to RBDs of the trimer and stabilize them in the closed state [10]. For example, a recent study shows that the naturally occurring fatty acid linoleic acid co-purified from certain cell lines binds tightly at three composite sites of the RBD trimers and thereby these interactions stabilize the closed state [10].

Whether and how small drug-like molecules can control the configuration of the RBDs remains largely unexplored. We find that the thio-conjugate of 3-oxo-valproate with coenzyme A (VPA-CoA) stabilizes the fully closed state of the trimer as shown by the structural characterization based on molecular dynamics (MD) simulations (Fig. 1, Supporting Fig. S1). The RBDs are stabilized in the "down" conformation by electrostatic interactions between the

negatively charged phosphate groups of VPA-CoA and the positively charged residues R408 of the three RBDs, and further so by a triple π-π stacking interaction that stabilizes the closed state of the RBDs (Fig. 1). VPA-CoA is a metabolic intermediate of valproic acid, a branched short-chain fatty acid found in plants and one of the most-prescribed medicines for the treatment of epilepsy, seizures, bipolar disorder, and migraine headaches [11–14]. VPA was first synthesized in 1881–1882 and accidentally came into medical use in 1962. However, there is no reported procedure for how to synthesize VPA-CoA chemically or biochemically for additional structural studies.

The approach introduced in this study is based on the stabilization of the closed RBD trimer by small drug-like molecules with dual effects. First, they stabilize the RBDs in a conformation that is not favorable for binding to the ACE2 receptors, thus allowing the immune system more time to neutralize the virus. Second, these molecules can serve as co-immunogens together with monomeric RBD immunogens of either mRNA-based or protein-based current vaccines by trimerizing the RBDs [15]. A recent study shows that the immunogens of trimer-stabilizing mutant spike proteins elicit a wholly different, but powerful class of non-ACE2 blocking neutralizing antibodies (NABs) [15]. The initial multiplication of the virus in an infected patient is likely to occur through a local cell-to-cell transmission that is not dependent on ACE2-RBD interactions [16]. This local spread of the virus through the respiratory tract may not be as dangerous as the long-distant spread to other essential organs [16]. Therefore, blocking this early step could be even more effective than ACE2-blocking NABs in long-distant cellular transmission. Many biochemical methods already exist to assess the

effectiveness of ACE2 blocking NABs [17], but those for non-ACE2 blocking NABs ought to be developed.

Significant efforts have been invested during the past two years to identify inhibitors that bind to the RBDs and block their interaction with the ACE2 receptor [18–20]. By targeting the protein-protein interaction, those inhibitors block the prefusion to postfusion state transition [1,21]. This is because the central stalk of the spike S2 fragment has the fusion peptides (FPs) that are buried in the pre-fusion state and exposed on the top of the extended stalk in the postfusion state. In the extended stalk, FPs are ready to insert into the host cell membranes to initiate the viral-host membrane fusion reaction. The distinct aspect of the approach introduced in this study is that the inhibitors do not directly compete for the spike-ACE2 protein-protein interaction but rather stabilize the RBDs in the closed conformation, which is unfavorable for interaction with the ACE2 receptor, opening a novel strategy based on the discovery of non-competitive molecular inhibitors.

2. Materials and methods

2.1. Grid-based docking

The complete 3-fold symmetric SARS-CoV-2 trimeric spike model was generated using the 6vxx coordinates (Fig. 1A) [22], and refined without glycosylation using the Protein Preparation Wizard workflow provided by Schrödinger suite with default parameter settings, including the assignment of bond orders, addition of H atoms, and assignment of partial charges at pH 7.0 [23,24]. After preprocessing, the structure was validated and minimized using the OPLS-2005 force field [25]. A grid was generated for docking, including all residues within a 20-Å radius of the central pore of the spike trimer. LigPrep [23] was used to prepare a total of 5811 compounds selected from the ZINC library [26], belonging to the categories of investigational, FDA-approved, or already approved drugs by equivalent authorities of other countries (Fig. 1C). A total of 16,576 targets were generated when as many as six tautomers per drug were considered at pH 7.0 ± 0.3. After the first step of high throughput virtual screening, which resulted in discarding 70 % of the targets, two docking methods (standard precision, SP, and extra precision, XP) were used for preliminary docking followed by a more accurate evaluation of the remaining 4972 leads (Fig. 1C) [27–30]. Compounds that failed to simultaneously bind the three RBDs were discarded. In this study we focus on VPA-CoA, which was among the compounds with the largest docking score and fulfilled the desired binding requirements. Other compounds, most of which are also VPA metabolites, emerged as promising candidates from the docking workflow and will be the subject of a subsequent study. The MD simulations described in this study probe VPA-CoA as a potential spike protein inhibitor capable of locking the spike trimer in the closed conformation through their specific interactions.

2.2. Modeling and MD simulations

The simulation models consist of a spike miniature complex (see next section for details) in the apo (ligand-free) state and in complex with VPA-CoA (placed at the interface between the RBD), using the docking pose as starting guess for dynamics. We ran MD simulations both using a miniature construct modeled from the WT spike trimer and using a variant sequence, which includes the K417/L452R/D950N mutations. Such mutations were sequentially accumulated on many variants of interest and mimicked the transition from Beta to Delta variants (Delta plus variant has an additional T478 mutation to K as a dominant form and to other residues as strain variants) [2,31,32]. Hence, the analysis reported here was primarily based on the K417/L452R/D950N trajectory. Figs. S2 and S3 in Supporting information show the analysis of dynamics of the spike central pore

for both this variant and WT (miniature) spike trimer over three 400 ns replicas, which demonstrated the efficiency of VPA-CoA in keeping the three RBD in a closed state, regardless of the mutations examined. This is not surprising given that the stitching action of VPA-CoA is widely contributed by the interaction between the drug and R408 residues, which belong to a cluster of highly conserved residues (N394–G416) [33], likely part of the triggering mechanism regulating the opening-and-closing dynamics surrounding at the central pore of the spike protein.

The structural model for the apo spike protein used in this study was obtained from the 3-fold symmetric structure as prepared for the docking calculations, retaining only the minimal number of atoms to ensure the stability of the trimeric assembly (residues Asn331-Pro527, Ser730-Val772, and Asn950-Ala1015). MD simulations of the resulting ligand-free and VPA-CoA bound spike constructs were based on the CHARMM36m force field for proteins [34], and Generalized Amber Force Field (GAFF) for the VPA-CoA ligand [35], as implemented in the NAMD software package [36–38]. Production run MD simulations were performed upon running a three-step pre-equilibration procedure: (i) hydrogen atoms with explicit TIP3 water solvent molecules (40,000 approximately) were added using VMD [39], and optimized, constraining the rest of the atoms at the initial structure positions, (ii) protein atoms and water were minimized and equilibrated for 150 ps using medium constraints (1 kcal/mol/Å² on the backbone and on the non-H ligand atoms and 0.5 kcal/mol/Å² on the non-H sidechain atoms), and (iii) all protein atoms were refined with medium constraints applied only between protein and non-H ligand atoms as in the starting structure. Each of the three equilibration steps included a 2Ps steepest descent minimization, followed by gradual heating and equilibration for the remaining steps up to a total of 50, 150, and 300 ps, respectively. Each of the equilibration MD simulations was performed in the canonical NVT (fixed amount, volume, and temperature) ensemble using Langevin dynamics. Unconstrained MD simulations were run for 5 ns, for a total pre-equilibration simulation time of 5.5 ns. Upon system pre-equilibration, MD simulations were performed in the NPT ensemble at 310 K and 1 atmosphere using the Langevin piston. Electrostatic interactions were accounted for using the Particle Mesh Ewald method [36], and van der Waals interactions were calculated using a cutoff of 12 Å and switching distance of 10 Å. All simulations were performed using periodic boundary conditions. A multiple time-stepping algorithm was utilized, where bonded, short-range non-bonded, and long-range electrostatic interactions were evaluated using a timestep of integration set to 2 fs [40].

Four independent 400 ns MD were carried out for (i) the ligand-free structure and (ii) VPA-CoA-bound complex using both WT and mutated sequence (K417N/L452R/D950N), for a total of 4.8 μs computed trajectories. The pore size (pairwise R408–R408 distances) across the three 400 ns replicas of both WT and mutant (K417N/L452R/D950N) ligand-bound trajectories insured stable holding of the drug over a longer trajectory, with a pore size significantly smaller than what found in the corresponding ligand-free trajectories. A comparison of the pore distance over three 400 ns replicas for both the ligand-free K417N/L452R/D950N variant and WT is provided in Supporting information (Fig. S3).

2.3. MD-derived ESP map calculation and analysis

For post-MD ESP analysis, we analyzed a total of 1000 frames, evenly spaced over the first 100 ns of each replica, using a procedure described elsewhere and briefly summarized as follows [41–43]. Each frame was aligned using the program *lsqkab* of the CPP4 suite for alignment [44], in reference to the Cα coordinates in the 6vxx structure and selecting either (i) each RBD singularly, or (ii) the three RBD subunits in a trimer, or (iii) upon centering of

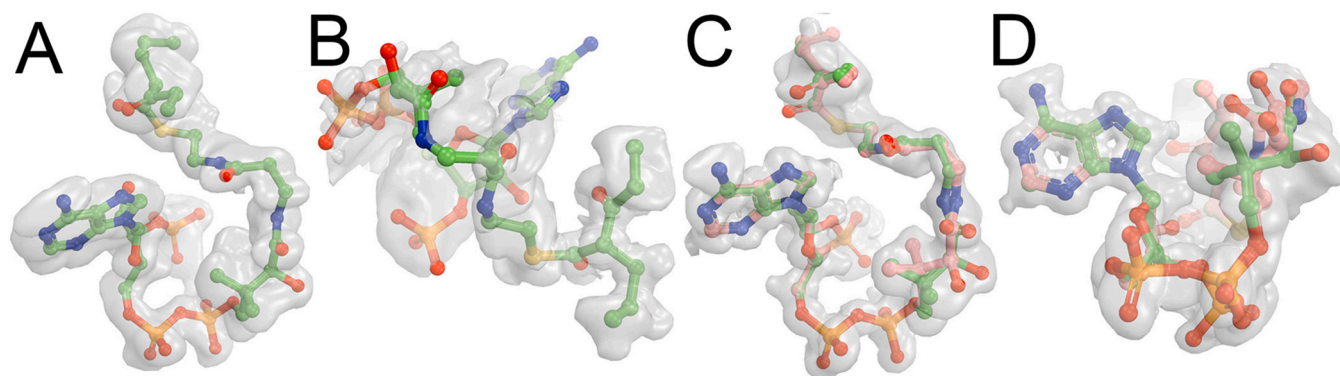


Fig. 2. MD-simulated conformations of the VPA-CoA molecule bound to the reduced model. (A–D) The VPA-CoA-only ESP maps contoured at 25σ after the drug atoms were aligned using all drug atoms (A), the valproate atoms only (B), and using 3',5'-ADP atoms. (C, D in two views). The pantothenic acid fragment of VPA-CoA has two alternate conformations (green and salmon, C, D).

the entire construct (at each frame) in a box of $120 \text{ \AA} \times 180 \text{ \AA} \times 160 \text{ \AA}$ (or smaller fixed boxes used for analysis of smaller fragments). All remaining calculations were carried out using the CCP4 suite [44]: (i) structure factors were calculated using *sfall* to 1.0 \AA with ΔB values of 8 \AA^2 added, (ii) maps were calculated using *fft* at the proper grid spacing and nominal resolution, and (iii) maps were averaged using *mapsig*. Equilibrated models were built using the graphics Coot into the resulting MD-derived ESP maps [45], and partially refined iteratively using Phenix and Refmac5 [46,47]. All figures were prepared using Pymol [48]. Inspection of the pore size across the remaining replicas ensured the ligand position was retained over time. An analysis of buried surface area was carried out using the program *arealmol* in CCP4 following the algorithm of Lee and Richards [44,49].

2.4. *gmx_MMPBSA* binding free-energy analysis

For calculating binding energies, we analyzed 100 frames of data, selected every 5 frames from 1000 to 1500 ns in the MD trajectory (with the validated most stable binding region of the ligand). Each frame was wrapped. Both water molecules and solvent ions were removed. The binding enthalpy was then calculated using *gmx_MMPBSA* package with the implicit solvent parameter set to be compatible with the corresponding protein and ligand forcefields [50]. The entropy term is not included due to the incompatibility between entropy analysis feature of *gmx_MMPBSA* package with *charmmFF*. The energy data for the obtained frames are reported for the mean and standard deviation.

2.5. Vector-difference Fourier maps for the spike protein between pH 4.5 and pH 4.0

The vector difference Fourier maps of the structures reported were determined using the experimental emd22515 map (pH 4.5, at 2.50 \AA resolution, PDB-7jwy) and emd22251 map (pH 4.0, at 2.40 \AA resolution, PDB-6xlu), referred to as "2P" mutated spike trimer for two prefusion state-stabilizing proline substitutions K986P/V987P [7]. These two maps were already on the same voxel scale and did not have a voxel scaling problem [51]. The structure factors were Fourier-inverted from these maps at 2.6 \AA resolution using Phenix [46], after the two maps were aligned and resampled on the same grids using Chimera [52]. They were scaled to remove resolution differences using the program *scaleit* of the CCP4 suite and vector-difference maps were calculated at 2.6 \AA resolution using the program of *fft* [44]. An overall amplitude difference between the two aligned maps after scaling was $\sim 20\%$ at 2.6 \AA resolution.

3. Results

3.1. Systematic search for lead compounds that close the RBDs

We conducted a systematic docking search analysis on over 5811 commercially available small molecules selected from the ZINC library database [26], belonging to the categories of 1379 US FDA-approved drugs, 2068 drugs approved by equivalent authorities in other countries, and 2364 investigational compounds not yet approved (Fig. 1). The grid-based docking procedure, illustrated in Fig. 1C and explained in detail in the Methods section, revealed several potential binders with docking scores above the ninetieth percentile of the overall distribution. A class of high-docking score binders that emerged from the docking workflow, was that of valproic acid derivatives (see Fig. S1 in Supporting information, SI). VPA-CoA was one of the top-ranking compounds including other valproic-acid metabolic derivatives, both according to the docking score and based on the number of non-covalent interactions formed with the receptor. Upon binding of VPA-CoA the RBDs of the spike trimer construct in this study, the trimer is in the closed conformation. The construct used in this study was derived from the spike trimer from the 3-fold symmetric and fully reconstructed 6vxx cryo-EM structure [22], including the RBD (Asn331-Pro527) and a short region from the S2 fragment (Ser730-Val772 and Asn950-Ala1015, for maintaining a trimer assembly) (Figs. 1A, 1B). For comparison and control computations, we ran MD simulations using both a miniature complex model for the wild-type (WT) sequence and a naturally occurring variant of interest that mimics an intermediate strain between Beta and Delta variants and includes the K417N/L452R/D950N mutations (see Section 2).

The energy-minimized structure of the ligand-free spike trimer has pseudo-3-fold symmetry. Nevertheless, atomic thermal fluctuations and asymmetric protein-ligand interactions typically break the symmetry of the three RBDs, which can be defined as distinct subunits A, B, or C (in salmon, gold, and blue in the figures, whenever possible). In the presence of a ligand, the three RBDs fluctuate and adopt asymmetric (open/closed) configurations as observed in MD simulations. Such observation is consistent with earlier studies showing substantial conformational heterogeneity in the open-closed dynamics [53].

3.2. Conformation of VPA-CoA during MD Simulations

VPA-CoA has many single bonds that are free to rotate when it is not bound to the protein but are mostly frozen when interacting with the spike trimer. Thus, the frozen conformation of VPA-CoA is

an essential condition for strong interactions between the VPA-CoA and the spike trimer. Our analysis of VPA-CoA conformations from MD simulations through ESP maps began with root-mean-squares fluctuations (rmsF) around the globally equilibrated structure. The rmsF values and thereby MD-derived ESP (MD-ESP) maps depend on how the molecule is aligned, for example, using all VPA-CoA atoms of the valproate fragment or using atoms of the 3',5'-ADP fragment only (Fig. 2). These maps indicate that both valproate and 3',5'-ADP fragments largely remain a rigid body throughout the MD simulations although the pantothenic fragment has two distinct conformations (Fig. 2). The VPA-CoA conformation that was fitted into these MD-ESP maps is largely identical to the starting rotamer conformation used for MD simulations.

Upon aligning each MD trajectory to the average position of the three RBDs, we found well-defined MD-ESP maps derived for both the spike trimer and bound rigid VPA-CoA, which reflect their equilibrated state (Fig. 3). We observed that the valproate tail fits well in a hydrophobic pocket of subunit C (Fig. 3B). Overall, the ESP map shows that VPA-CoA is bound at the center of three RBDs involving multiple H-bonds with the spike trimer, including H-bonds with the three R408 residues one from each spike subunit as well as with D405 and Y508 from subunit B (Fig. 3). The equilibrated structure is very similar to the starting structure, in a situation that differs from several other lead compounds in that a large translation over 10 Å has been observed from an early stage of the MD simulations to the finally equilibrated positions. However, the RBD trimer rotates relative to the trimeric S2 fragment (SI text, Fig. S4), i.e.,

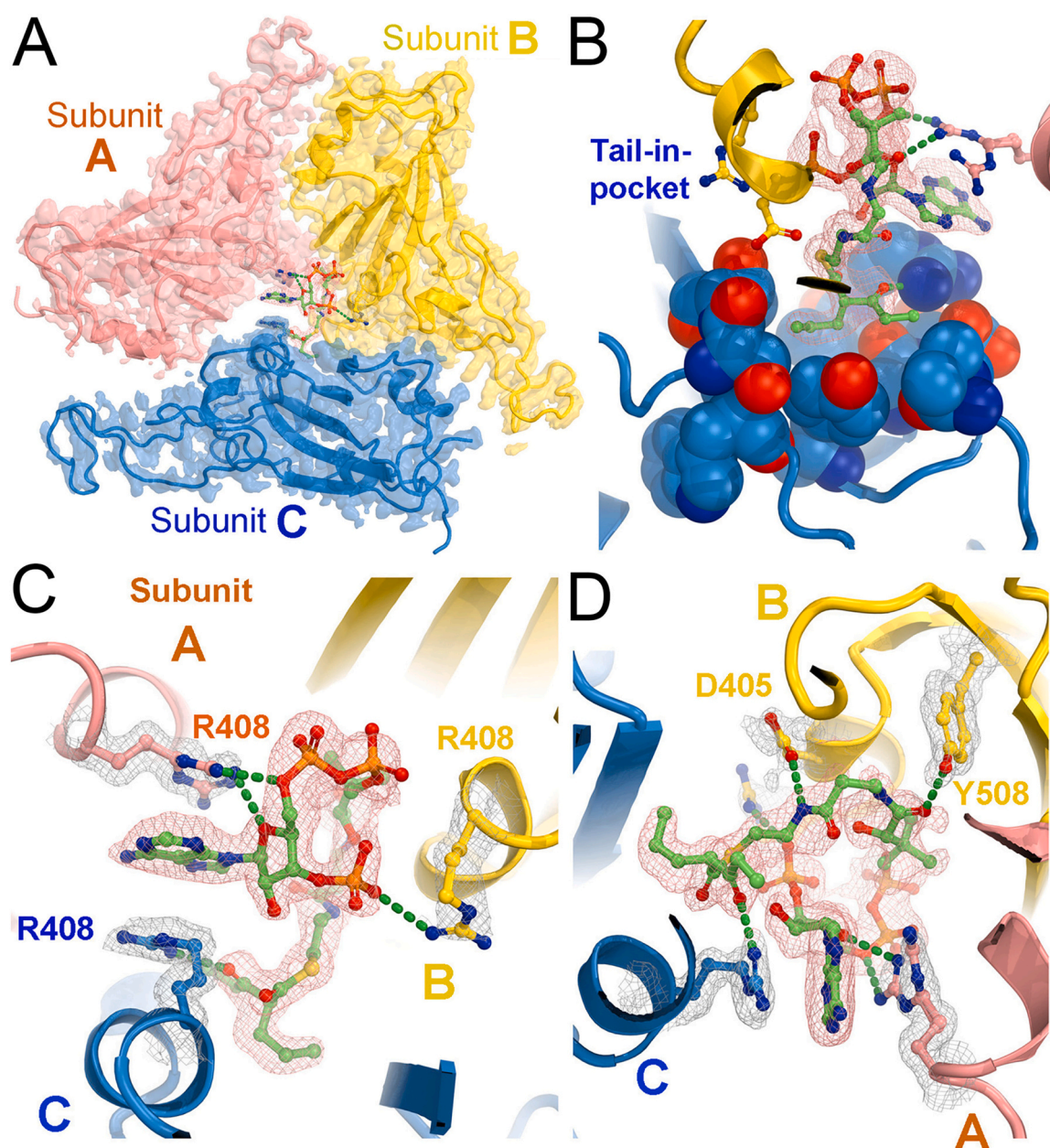


Fig. 3. MD-simulated structures of the VPA-CoA molecule bound to the miniature construct and its interactions with the RBD trimers. (A) After three RBD C α atoms were aligned, MD-ESP maps are contoured at 4 σ and colored by domains in cartoon drawing and VPA-CoA in green balls-and-sticks. (B–D) Three RBD-aligned MD-ESP maps contoured at +4 σ carved for the drug (salmon iso-meshes) and for three R408 residues (silver iso-meshes) in three view orientations, highlighting packing the tail valproate group within a hydrophobic pocket of subunit C (B), stacking interactions between two R408 residues flanking the adenosine base (C), and H-bonding interactions with D405 and Y508 of subunit B (D).

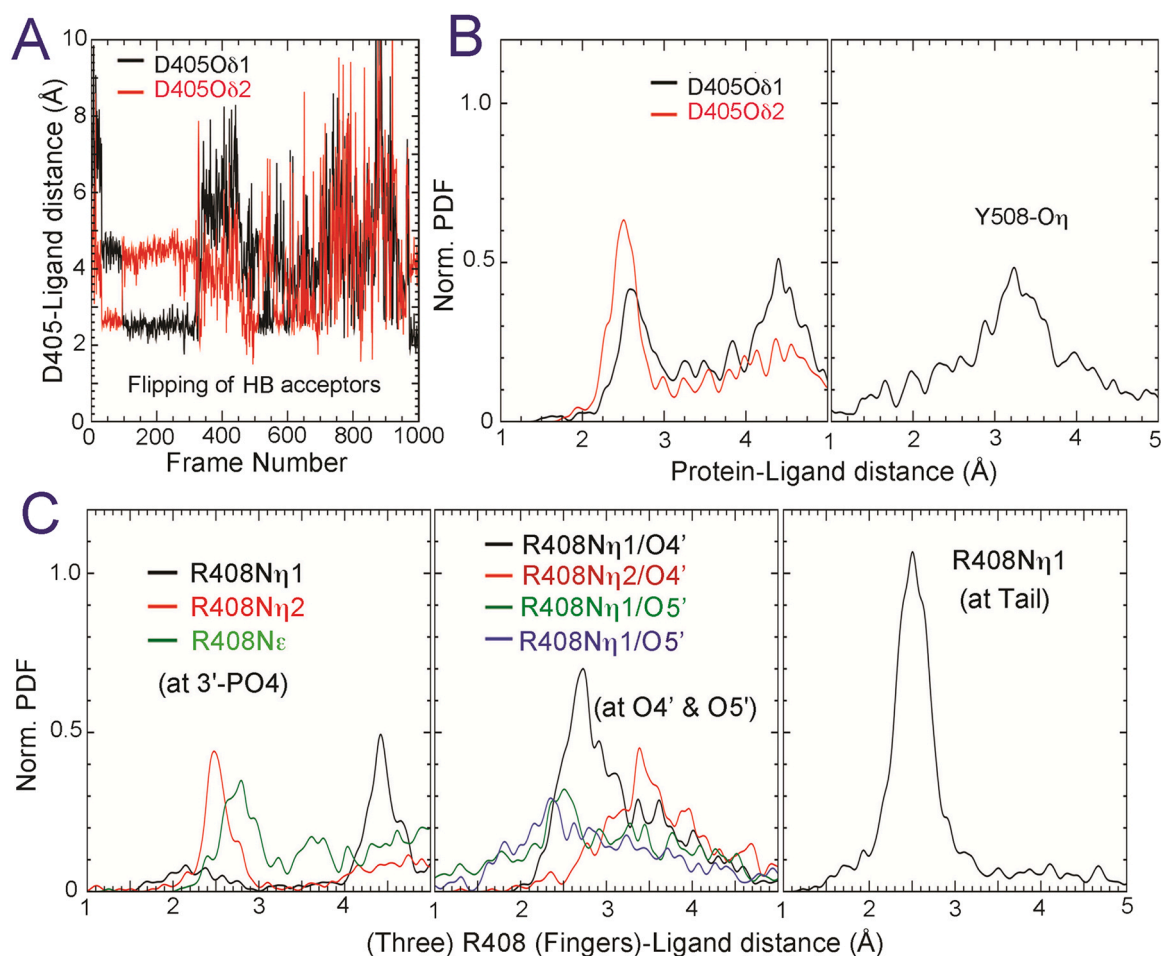


Fig. 4. Interatomic protein-VPA-CoA distances in MD trajectories and their distribution. (A) Between D405Oδ1/D405Oδ2 and the amine N atom of its β -mercapto-hydroxylamine fragment as a function of MD trajectory frame. (B) Normalized PDFs for D405, and for Y508O η to a hydroxyl of its pantothenic fragment. (C) Normalized PDFs for R408 to the 3'-PO $_4$ group of the 3',5'-ADP fragment of VPA-CoA, for R408 to the O4' and O5' atoms of the 3',5'-ADP fragment, and for R408 to the keto carbonyl of its valproate fragment.

interactions between RBD trimer and S2 trimer in our systems are not conserved throughout MD simulations.

3.3. VPA-CoA closes the central pore of the spike trimer

We find that binding of VPA-CoA shortens the pairwise inter-subunit C α -C α distances between residues R408 by about 1.0 Å per pair, shrinking the central pore radius by about 0.87 Å (as shown in Fig. S2 in SI). Pairwise R408-R408 C α distances are 13.2 Å, 14.9 Å, and 17.2 Å in the asymmetric RBDs/VPA-CoA complex with the mean value of 15.1 ± 1.6 Å, significantly smaller than the corresponding 16.1 Å distance in the 3-fold symmetric 6vxx closed structure [22].

VPA-CoA makes specific interactions with the three R408 residues one from each RBD in addition to the complementary electrostatic interaction between the negatively charged phosphate groups of VPA-CoA and the positively charged R408 residues (Fig. 3). Two R408 residues stack against both faces of the adenine of CoA known as a cation- π interaction or a triple π - π stacking, an occurrence that is well documented for other CoA conjugate structures [54–57]. In addition, H-bonds of various moieties of VPA-CoA are maintained with the RBDs, including those with the 3'-phosphate, the O4'/O5' of the 3',5'-ADP fragment, and the keto carbonyl group on the valproate fragment. The amide of the β -mercapto-hydroxylamide fragment is H-bonded to D405 and the non-chiral hydroxyl group (or the keto form in a keto-enol equilibrium) is weakly H-bonded to Y508, both in subunit B. Particularly, the H-bond between R408 N η 1 of subunit C and the keto carbonyl of the valproate

fragment is very stable and persists throughout the entire MD simulation, while its sidechain stacks against the adenosine base of VPA-CoA (Fig. 4). The guanidinium fragment of this arginine residue does not appear to flip whereas the other two R408 residues are rapidly flipping throughout the MD trajectory (Fig. 4C). The interaction of the valproate acid with an arginine sidechain was also observed in other systems [58]. The flexible displacement of the entire guanidinium group of an arginine residue around the rotatable Ce-N ζ bond requires significant space compared to that occupied by freely rotating Asp and Glu terminal groups, such that the motion of arginine's sidechains is highly coupled with that of neighboring residues such as D405 (Fig. 4A, B). The H-bonding interaction of Y508 is relatively weak, with the peak probability of distance distribution at 3.2 Å, compared to the R408/valproate carbonyl group interaction with the maximal probability of distance at 2.5 Å.

Six new inter-subunit H-bonds are formed between subunits A and B, due to the pore shrinking upon binding of VPA-CoA to the RBD trimer, including Y589O η -D364Oδ2, Asn417Nδ2-Asn370Oδ1, Y453O η -A372N, R403N η 1-Phe374N, Y505O η -Ser375O γ , and Thr500O-Asn440Nδ2 (Fig. 5). These H-bonds are not observed between other pairs of subunits in either the VPA-CoA complex or the ligand-free structure described below, or the symmetric 6vxx closed structure. These H-bonds are interspersed by hydrophobic interactions, which in turn increase the strength of the H-bonds (Figs. 5C, 5D). These interactions explain why the closed state of the VPA-CoV complex observed here in our MD simulations is even closer than the

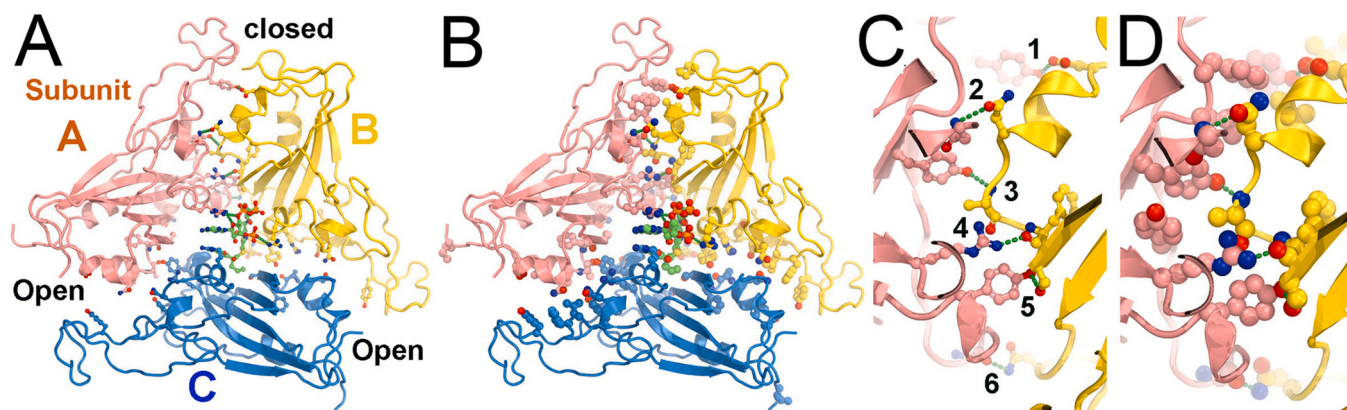


Fig. 5. VPA-CoA induced subunit interactions of the RBD trimer. (A) Six inter-subunit H-bonds only between subunits A and B, but not between A and C or between B and C. (B) Other hydrophobic residues buried at the interface between A and B. (C, D) A close-up view of (A, B). Six pairs of inter-subunit H-bonds are: [1] Y589O η -D364O δ 2, [2] Asn417N δ 2-Asn370O δ 1, [3] Y453O η -A372N, [4] R403N η 1-Phe374N, [5] Y505O η -Ser375O γ , and [6] Thr500O-Asn440N δ 2.

6vxx closed structure observed experimentally but without a ligand. The closing of the central pore of the RBDs upon binding of VPA-CoA relative to the apo MD trajectories can be seen in the R408-R408 pair distance throughout the MD frames and corresponding the probability distribution density (PDF) (Fig. 6).

Triangulation of three sets of the inter-subunit R408C α -R408C α distances (i.e., between subunits A and B, B and C, and C and A) provides an estimate for the size of the central pore of the RBD trimer in MD trajectories (Fig. 7). The R408-to-R408 distances are plotted as a function of trajectory frame number (and as probability density functions PDF). The mean values for the three sets of the

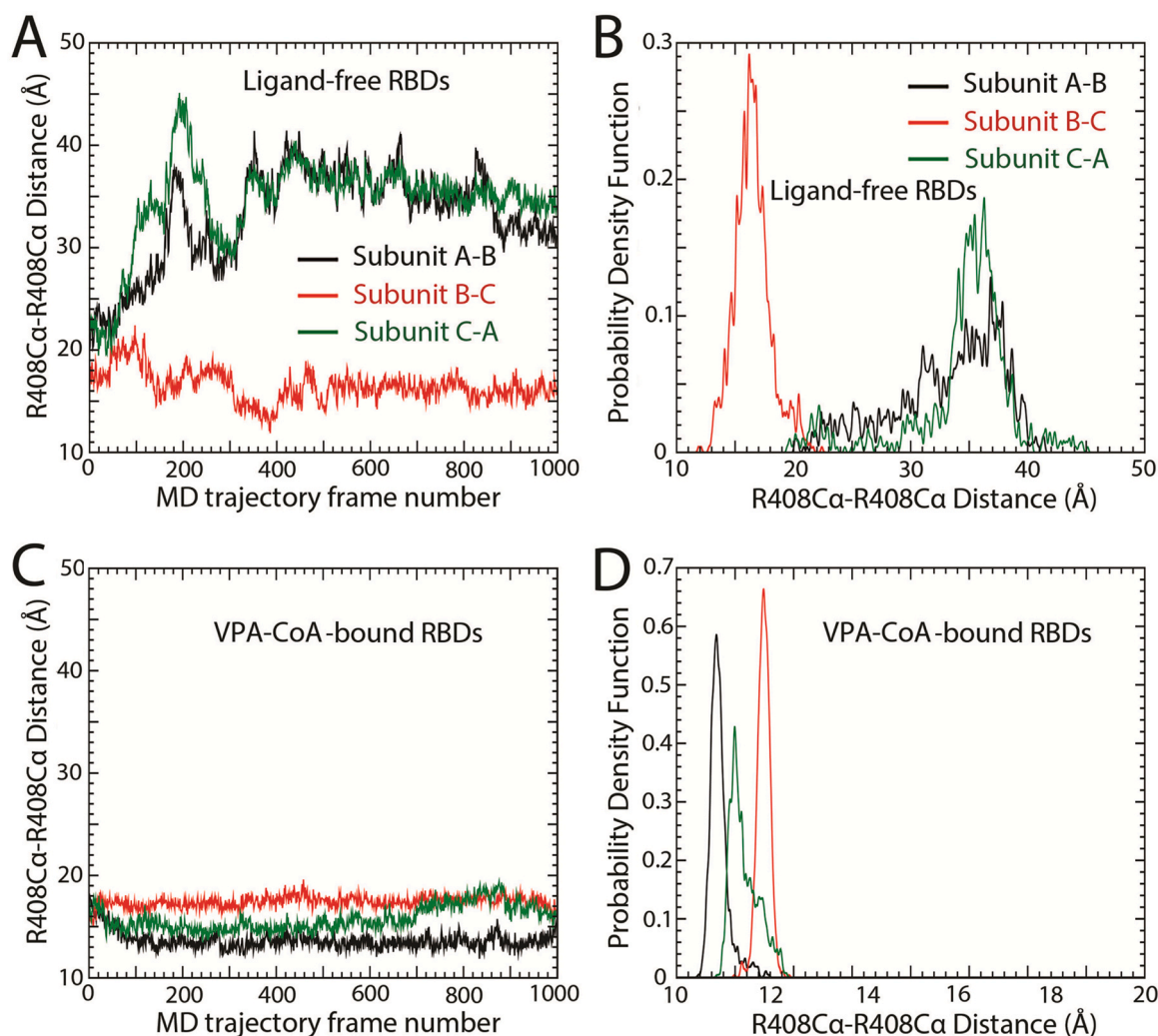


Fig. 6. Inter-subunit inter-atomic R408C α -R408C α distances in MD trajectories of the ligand-free RBD trimers (A, B), and in the VPA-CoA/trimeric RBD complex (C, D). They are plotted as a function of MD simulation trajectory film (A, C) or as probability density functions (B, D).

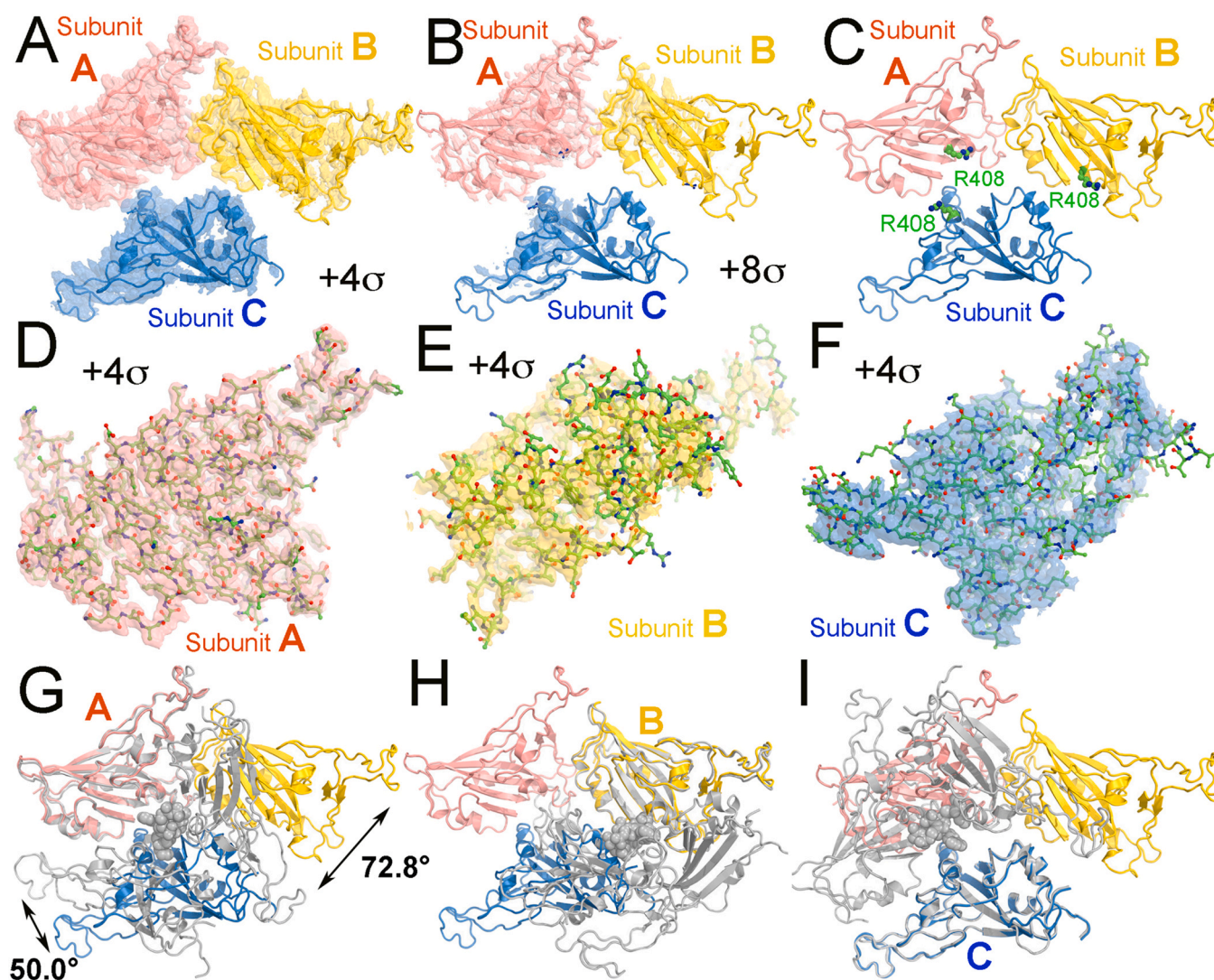


Fig. 7. The ligand-free structure of three RBDs and its comparison with the VPA-CoA bound structure. (A, B) Maps contoured at 4σ (A) or 8σ (B) after the three RBD atoms were aligned, colored by subunits. (C) Highlighting three R408 residues in the subunits. (D–F) Maps for three individual RBDs in selected orientation views. (G–I) Alignment of three RBDs (salmon, gold, and blue) of the ligand-free structure with the VPA-CoA bound (silver) with alignment of α of subunit A (G), subunit B (H), or subunit C (I).

interatomic distances in the ligand-free RBD trimers (see below) are 33.1 ± 4.7 Å, 16.5 ± 1.5 Å, and 34.5 ± 4.4 Å, respectively, with an average value of 28.0 ± 9.0 Å. In the VPA-CoA bound complex, they are 13.7 ± 0.8 Å, 14.9 ± 0.5 Å, 15.8 ± 1.2 Å, respectively, with an average value of 15.6 ± 1.8 Å. These values are comparable to those measured from the corresponding equilibrated structures. To confirm the persistency of the pore-closing effect exerted by the drug we examined the pore distances across longer simulations, throughout three 400 ns replicas, confirming the tendency of drug-bound simulations to sample much fewer open-pore configurations compared to what is observed in the WT ligand-free MD simulations (see Fig. S3 in SI).

3.4. Buried surface areas in the VPA-CoA/RBD complex and free energy estimation

The buried surface area between subunits A and B is 797 Å² in the equilibrated structure derived from the entire MD trajectories, while the buried surfaces of the two other pairs of subunits are 282 and 312 Å², respectively. According to the classic Chothia-Janin model [59], the binding energy between two subunits is linearly proportional to the buried surface area, i.e., $\Delta G_{\text{binding}} = -k\Delta A$, where $k = 0.025$ kcal/mol/Å² for buried hydrophobic surfaces. Therefore, the

estimated hydrophobic binding affinity is -19.9 kcal/mol further stabilizing seven H-bonds established between subunits A and B. The surface area buried between VPA-CoA and the RBD trimer is 655 Å², which represents 68 % of the total surface of VPA-CoA and corresponds to -16.4 kcal/mol, which had not included in the binding-energy estimation of 5 H-bonds between VPA-CoA and the RBD trimer. Therefore, VPA-CoA greatly stabilizes the interactions between subunits A and B.

The above simple energy estimation is comparable in accuracy and reliability with some of more expensive calculations from equilibrium structures derived from MD-simulations combined with additional energy minimization, such as Molecular Mechanics Generalized Born Solvation Area Model as implemented in the AmberTools20 package [60,61]. The procedure is known to provide reliable free energy of complex formation between the spike trimer and multiple ACE2 receptors allosterically after energy minimization with the PMEMD (also part of the Amber package) as we have recently demonstrated [62]. Unfortunately, that package is not compatible with our current MD simulation parameters so that we had to select MMPBSA package for as an alternative [50].

MMPBSA method works well for estimating of binding enthalpy of a typical ligand into a relatively stable pocket of a monomeric receptor in two steps in individual frames of MD trajectories

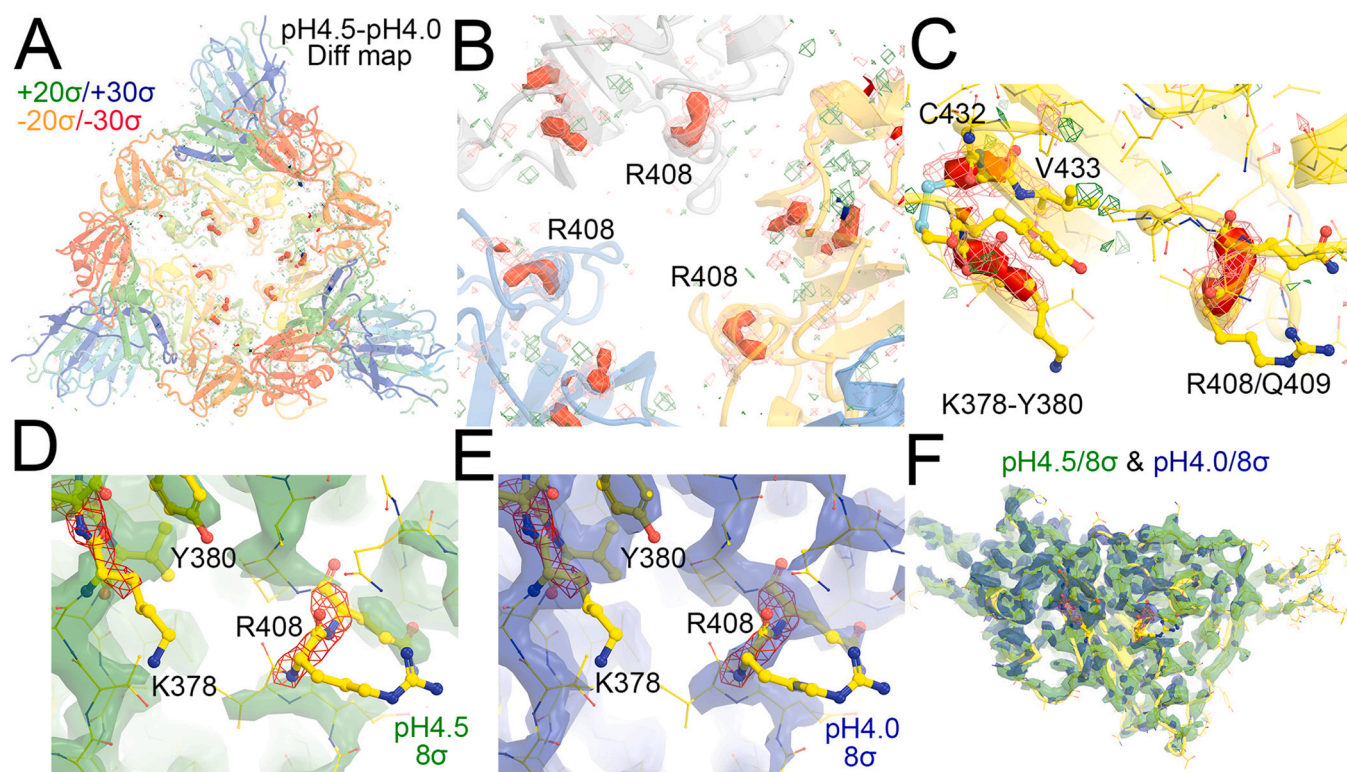


Fig. 8. Vector-difference ESP features between emd22515 (pH 4.5 for "2P" mutated spike trimer/PDB 7jwy) and emd22521 (pH 4.0 for "2P" mutated spike trimer/PDB 6xlu). (A–C) Successive close-up views of difference maps for the entire S1 fragment trimer contoured at both high ($\pm 30\sigma$, blue and red) and low ($\pm 20\sigma$, green and salmon). (D) Superposition of pH 8.0 ESP map at 8σ (green isosurfaces) with the difference features (isomeshes) and coordinates exhibits gaps at the R408–Q409 and K378–Y380, and C432–V433 backbones. (E) The pH 4.0 map (blue isosurfaces) does not have these gaps at this contour level. (F) The RBD of the spike protein with both pH 8.0 (green) and pH 4.0 (blue) maps are superimposed.

followed by averaging throughout all frames, (i) the binding energy in vacuum by calculating the differences between the ligand-receptor complex and sum of the isolated receptor and the isolated ligand, and (ii) the corresponding differences of their hydration energy with an implicit solvent model parameterized for the corresponding force field [50]. However, when we applied this method for binding energy calculation after the method carved out either the RBD trimer as receptor or VPA-CoA ligand as ligand out of the complex in MD trajectories, we found surprisingly that the net binding energy estimated is $+20.4 \pm 5.2$ kcal/mole. This finding is not consistent with our MD observation where VPA-CoA binds throughout 100 ns MD trajectories largely in the same position as revealed by MD-derived ED maps. Possible explanations of this inconsistency are as follows: (i) carved RBD trimers has major differences in terms of conformations compared with the apo RBD trimer, and this invalidates the basic assumption made by MMPBSA, (ii) some of VPA-CoA binding energy has been transferred to stabilize the RBD trimer in the closed conformation, and (iii) when ligand is dominantly hydrophilic like CoA conjugates, the entropy term, which is not feasible form in the current method with charmmFF, would play a larger role to the total free energy, which we have not accounted for. The entropy associated with simultaneous binding of the ligand to multiple RBDs has not been included in this calculation. In general, this method has some limitations for our system. Therefore, new methodology needs to be developed for resolution of these issues because we will continue to search for other CoA conjugates for tighter binding both computationally and experimentally.

3.5. The apo or ligand-free state of the RBD trimer

The equilibrated subunit structure of the spike trimer that has been fitted into the MD-ESP map is essentially identical to the

starting subunit structure although the quaternary structure differs, i.e., the motions of the spike trimer is largely rigid-body with small fluctuations around the equilibrated position (Fig. 6). We note that the ligand-free or apo structure has well-defined ESP features only at low contouring level while the VPA-CoA bound complex exhibits well-defined ESP features for the three subunits in both low and high-contouring levels of $+4\sigma$ and $+8\sigma$. To address whether the RBDs move as individual rigid bodies or are partially unfolded throughout MD trajectories in the apo structure, we selected each RBD, aligned it, and calculated its ESP map. The resulting MD-ESP maps of each subunit showed that the RBDs remain largely rigid-body motions during MD simulations and that they do not unfold during the MD simulations. Therefore, the apo structure has a larger amplitude of rigid-body motions than the complex structure.

Two of the RBDs (i.e., subunits A and B) in the apo structure have closer contact with each other than with the other RBD in the trimer. The third subunit C is relatively more hydrated and interacts less with neighbors than subunits A or B. However, the interface between the two closely interacting subunits A and B in the apo structure is significantly different from the corresponding interface in the VPA-CoA complex. Such asymmetric conformations bear some similarity to that found in other MD simulations reported in the literature. For example, the overall conformation of the apo RBD trimer is close to that found in replica 2 of a ~ 573 ns MD simulation of the full-length spike trimer reported by the Amaro group [3].

Comparison of the orientations of the spike subunits in the VPA-CoA complex and in the apo structure shows that when one subunit was aligned, the remaining subunits rotated by as much as $\sim 73^\circ$ (Fig. 6G). This observation supports our hypothesis that the binding of VPA-CoA alters the distribution of configurations of the RBDs in the trimer.

3.6. R408 and K378 as part of pH-dependent triggering mechanisms

The pairwise R408–R408 distances corresponding to the fluctuating configurations of the RBD subunits in the ligand-free trimer differ by more than 20 Å along the MD simulations in two pairs, and 12 by Å overall for all three pairs. We rationalize such spatial separation between the RBD domains as resulting from the repulsive interactions that occur between the positively charged R408 residues near the central pore of the RBD trimer. Such motion is suppressed upon binding of VPA-CoA that simultaneously interacts with the side chains of R408 from each of the three RBD subunits, locking the spike trimer in the closed conformation.

We selected the central pore of the RBDs for drug discovery in this study, including R408, because (i) three R408 residues are close to the 3-fold axis in the symmetric, closed structure and would have excessively positive ESP values, (ii) R408 belongs to a cluster of highly conserved residues among beta-coronaviruses, referred previously as the RBD.4 motif, including residues N394–G416 [33], and (iii) R408 is conserved in all variants examined. The cluster of three positively charged R408 residues of the three RBDs plus three K378 residues (highly positive ESPs) away from the central axis interact with a cluster of 24 negatively charged carboxylates in the S2 fragment at neutral pH (D985, E988, E990, D994, D737, D745, E748, and D979) (highly negative ESPs) and only 6 positively charged residues (R983 and R995) of S2 in an intricate long-range ESP network. These carboxylates can serve as pH sensors and be fully or partially protonated at low pH conditions. They are clustered together within a small space like a loaded spring in the prefusion state of S2 fragment and dispersed in a much larger space in the postfusion state.

Our analysis of vector-difference Fourier maps (see Methods) between two cryo-EM maps recently reported [7] at pH 4.5 and pH 4.0 clearly shows that the R408 and K378 clusters are part of the triggering mechanism that controls the prefusion-to-postfusion state transition, as revealed by the pH dependent change of the total ESP values (Fig. 8). With an increased pH by 0.5 unit from pH 4.0 to pH 4.5, the cumulative effect is amplified from partial deprotonation of many carboxylates that extends to their surrounding environment, resulting in significant loss of ESP values in both positively charged residues, which were only two significant difference features per subunit in the trimer of the S2 fragment at both the R408 and K378 residues (Fig. 8). Therefore, interactions between the S1 and S2 trimers and the opening and closing of the central pore of the S1 trimer are regulated by long-range ESPs.

4. Discussion

Our MD simulations provide clear evidence that VPA-CoA stabilizes the closed conformation of RBDs (all three in down positions) in the SARS-CoV-2 spike trimer by binding simultaneously to residues of the three RBDs. Therefore, VPA-CoA suppresses the opening of RBDs that is critical to expose its RBMs for binding to the ACE-2 receptor. This suppression does not compete for specific binding sites of the ACE-2 receptor on the RBMs. Thus, VPA-CoA is a non-competitive allosteric inhibitor. Molecular interactions between the VPA-CoA conjugate and the RBD trimers involve specific H-bonding, complementary electrostatic, and hydrophobic stacking interactions. Given the mechanistic conservation of R408 as part of triggering mechanism for a loaded spring of the spike protein trimer, non-competitive allosteric inhibitors such as the VPA-CoA conjugate identified in our study should be relevant to a broad spectrum of SARS-CoV-2 variants and all variants of Beta-CoVs.

We anticipate that other CoA-fatty acid conjugates could maintain analogous interactions to those observed between VPA-CoA and the RBD trimer. In fact, all other valproic acid metabolites emerged among the top-ranked non-peptide compounds from the docking workflow, with similar interaction profiles in the docking pose,

involving residues S375, T376, K378, R408, V503, G504, and Y508. Another important class of compounds suggested by the docking is that of tetra-phosphate nucleotide analogs that also electrostatically interact with the positively charged R408 residues in each of the three RBDs of the trimer, revealing a new type of chemical group for incorporating into a pharmacophore that stabilizes the down, inactive conformation of the RBDs.

Our observation of specific interactions observed between the CoA conjugates and the RBDs of the spike trimer leads to a tantalizing speculation that cellular fatty acid-CoA conjugates could be able to partially inhibit the spike activation by stabilizing the prefusion state during the virion maturation step. The conjugates, however, could be stripped off by the host membrane because cellular fatty acid CoA conjugates are typically not membrane permeable. In fact, the serendipitous observation of binding of copurified linoleic acid to some of the purified spike proteins in certain cell lines highlights a potential problem of stripping off important cofactors from the spike protein in other cell lines [10]. In that case, the fatty acid CoA conjugates could function as a 'staple' that locks the RBDs of the spike trimer in a loaded spring-like state during virion maturation. Therefore, modified CoA conjugates as discovered in this study could disable the membrane fusion mechanism as allosteric inhibitors of conformation changes of the spike trimer, particularly those of naturally occurring intermediates of fatty acid degradations once we have established principles of ligand-spike protein interactions. This could open a new avenue to attenuate coronaviruses.

CRediT authorship contribution statement

F.M and T.Q. built the models and ran molecular dynamics simulations. J.W. and F.M. constructed the methodology performed the simulation analyses and wrote the draft manuscript. V.S.B and J.W. oversaw the research project. E.L. and G.P.L. contributed to the conceptualization of the work along with J.W. and V.S.B. All authors contributed to the final version of the manuscript.

Conflict of interest statement

Authors declare no conflict of interest in publishing this study.

Acknowledgments

This work was supported by the NIH Grant GM106121 (VSB), by the NIH Grant R01GM136815 (VSB and GPL), and by a generous allocation of high-performance computing time from NERSC.

Appendix A. Supporting information

Supplementary data associated with this article can be found in the online version at [doi:10.1016/j.csbj.2023.01.014](https://doi.org/10.1016/j.csbj.2023.01.014).

References

- [1] Li F. Structure, function, and evolution of coronavirus spike proteins. *Annu Rev Virol* 2016;3:237–61.
- [2] Harvey WT, et al. SARS-CoV-2 variants, spike mutations and immune escape. *Nat Rev Microbiol* 2021;19:409–24.
- [3] Casalino L, et al. Beyond shielding: the roles of glycans in the SARS-CoV-2 spike protein. *ACS Cent Sci* 2020;6:1722–34.
- [4] Ke Z, et al. Structures and distributions of SARS-CoV-2 spike proteins on intact virions. *Nature* 2020;588:498–502.
- [5] Ye G, Liu B, Li F. Cryo-EM structure of a SARS-CoV-2 omicron spike protein ectodomain. *Nat Commun* 2022;13:1214.
- [6] Diaz-Salinas MA, et al. Conformational dynamics and allosteric modulation of the SARS-CoV-2 spike. *Elife* 2022;11.
- [7] Zhou T, et al. Cryo-EM structures of SARS-CoV-2 spike without and with ACE2 reveal a pH-dependent switch to mediate endosomal positioning of receptor-binding domains. *Cell Host Microbe* 2020;28(867–879):e865.
- [8] V'kovski P, Kratzel A, Steiner S, Stalder H, Thiel V. Coronavirus biology and replication: implications for SARS-CoV-2. *Nat Rev Microbiol* 2021;19:155–70.

- [9] Pizzato M, et al. SARS-CoV-2 and the host cell: a tale of interactions. *Front Virol* 2022;12:815388.
- [10] Toelzer C, et al. Free fatty acid binding pocket in the locked structure of SARS-CoV-2 spike protein. *Science* 2020;370:725–30.
- [11] Loscher W. Basic pharmacology of valproate: a review after 35 years of clinical use for the treatment of epilepsy. *CNS Drugs* 2002;16:669–94.
- [12] Naliavaeva NN, Belyaev ND, Turner AJ. Sodium valproate: an old drug with new roles. *Trends Pharm Sci* 2009;30:509–14.
- [13] Ferreira JP, Oliveira AC, Saraiva FA, Vasques-Novoa F, Leite-Moreira A. Sodium-glucose co-transporter inhibitors in insulin-treated diabetes: a meta-analysis. *Eur J Endocrinol* 2021;184:783–90.
- [14] Johannessen CU, Johannessen SI. Valproate: past, present, and future. *CNS Drug Rev* 2003;9:199–216.
- [15] Carnell GW, et al. SARS-CoV-2 spike protein stabilized in the closed state induces potent neutralizing responses. *J Virol* 2021;95:e0020321.
- [16] Zeng C, et al. SARS-CoV-2 spreads through cell-to-cell transmission. *Proc Natl Acad Sci USA* 2022;119.
- [17] Ravichandran S, et al. Antibody signature induced by SARS-CoV-2 spike protein immunogens in rabbits. *Sci Transl Med* 2020;12.
- [18] Wang L, et al. Discovery of potential small molecular SARS-CoV-2 entry blockers targeting the spike protein. *Acta Pharm Sin* 2021. 10.1038/s41401-021-00735-z.
- [19] Basu A, Sarkar A, Maulik U. Molecular docking study of potential phytochemicals and their effects on the complex of SARS-CoV2 spike protein and human ACE2. *Sci Rep* 2020;10:17699.
- [20] Gorgulla C, et al. A multi-pronged approach targeting SARS-CoV-2 proteins using ultra-large virtual screening. *iScience* 2021;24:102021.
- [21] Kirchdoerfer RN, et al. Pre-fusion structure of a human coronavirus spike protein. *Nature* 2016;531:118–21.
- [22] Walls AC, et al. Structure, function, and antigenicity of the SARS-CoV-2 spike glycoprotein. *Cell* 2020;183:1735.
- [23] Bioluminate. New York, NY: Schrödinger.
- [24] Woo H, et al. Developing a fully glycosylated full-length SARS-CoV-2 spike protein model in a viral membrane. *J Phys Chem B* 2020;124:7128–37.
- [25] Shivakumar D, Harder E, Damm W, Friesner RA, Sherman W. Improving the prediction of absolute solvation free energies using the next generation OPLS force field. *J Chem Theory Comput* 2012;8:2553–8.
- [26] Irwin JJ, Sterling T, Mysinger MM, Bolstad ES, Coleman RG. ZINC: a free tool to discover chemistry for biology. *J Chem Inf Model* 2012;52:1757–68.
- [27] Good AC, Krystek SR, Mason JS. High-throughput and virtual screening: core lead discovery technologies move towards integration. *Drug Discov Today* 2000;5:61–9.
- [28] Friesner RA, et al. Extra precision glide: docking and scoring incorporating a model of hydrophobic enclosure for protein-ligand complexes. *J Med Chem* 2006;49:6177–96.
- [29] Halgren TA, et al. Glide: a new approach for rapid, accurate docking and scoring. 2. Enrichment factors in database screening. *J Med Chem* 2004;47:1750–9.
- [30] Friesner RA, et al. Glide: a new approach for rapid, accurate docking and scoring. 1. Method and assessment of docking accuracy. *J Med Chem* 2004;47:1739–49.
- [31] Mannar D, et al. Structural analysis of receptor binding domain mutations in SARS-CoV-2 variants of concern that modulate ACE2 and antibody binding. *Cell Rep* 2021;37:110156.
- [32] Saville JW, et al. Structural and biochemical rationale for enhanced spike protein fitness in delta and kappa SARS-CoV-2 variants. *Nat Commun* 2022;13:742.
- [33] Trigueiro-Louro J, Correia V, Figueiredo-Nunes I, Giria M, Rebelo-de-Andrade H. Unlocking COVID therapeutic targets: a structure-based rationale against SARS-CoV-2, SARS-CoV and MERS-CoV spike. *Comput Struct Biotechnol J* 2020;18:2117–31.
- [34] Huang J, et al. CHARMM36m: an improved force field for folded and intrinsically disordered proteins. *Nat Methods* 2017;14:71–3.
- [35] Ozipinar GA, Peukert W, Clark T. An improved generalized AMBER force field (GAFF) for urea. *J Mol Model* 2010;16:1427–40.
- [36] Phillips JC, et al. Scalable molecular dynamics with NAMD. *J Comput Chem* 2005;26:1781–802.
- [37] Phillips JC, et al. Scalable molecular dynamics on CPU and GPU architectures with NAMD. *J Chem Phys* 2020;153.
- [38] Acun B, Buch R, Kale LV, Phillips JC. NAMD: scalable molecule dynamics based on the CHARM++ parallel runtime system. Exascale scientific applications: scalability and performance portability; 2017.
- [39] Humphrey W, Dalke A, Schulten K. VMD: visual molecular dynamics. *J Mol Graph* 1996;14(33–38):27–38.
- [40] Grubmüller H, Heller H, Windemuth A, Schulten K. Generalized verlet algorithm for efficient molecular dynamics simulations with long-range interactions. *Mol Simulat* 1991;6:121–42.
- [41] Wang J, et al. Insights into binding of single-stranded viral RNA template to the replication-transcription complex of SARS-CoV-2 for the priming reaction from molecular dynamics simulations. *Biochemistry* 2022;61:424–32.
- [42] Wang J, et al. Structural basis for reduced dynamics of three engineered HNH endonuclease Lys-to-Ala mutants for the clustered regularly interspaced short palindromic repeat (CRISPR)-associated 9 (CRISPR/Cas9) enzyme. *Biochemistry* 2022;61:785–94.
- [43] Wang J, et al. Structural insights into binding of remdesivir triphosphate within the replication-transcription complex of SARS-CoV-2. *Biochemistry* 2022;61:1966–73.
- [44] Winn MD, et al. Overview of the CCP4 suite and current developments. *Acta Crystallogr D Biol Crystallogr* 2011;67:235–42.
- [45] Emsley P, Cowtan K. Coot: model-building tools for molecular graphics. *Acta Crystallogr D Biol Crystallogr* 2004;60:2126–32.
- [46] Adams PD, et al. PHENIX: a comprehensive python-based system for macromolecular structure solution. *Acta Crystallogr D Biol Crystallogr* 2010;66:213–21.
- [47] Murshudov GN, Vagin AA, Dodson EJ. Refinement of macromolecular structures by the maximum-likelihood method. *Acta Crystallogr D Biol Crystallogr* 1997;53:240–55.
- [48] Delano WL. Pymol. Schrödinger, Inc. (<http://pymol.org/>).
- [49] Lee B, Richards FM. The interpretation of protein structures: estimation of static accessibility. *J Mol Biol* 1971;55:379–400.
- [50] Valdes-Tresanco MS, Valdes-Tresanco ME, Valiente PA, Moreno E. gmx_MMPBSA: a new tool to perform end-state free energy calculations with GROMACS. *J Chem Theory Comput* 2021;17:6281–91.
- [51] Wang J, et al. How to correct relative voxel scale factors for calculations of vector-difference Fourier maps in cryo-EM. *J Struct Biol* 2022;214:107902.
- [52] Pettersen EF, et al. UCSF Chimera – a visualization system for exploratory research and analysis. *J Comput Chem* 2004;25:1605–12.
- [53] Zimmerman MI, et al. SARS-CoV-2 simulations go exascale to predict dramatic spike opening and cryptic pockets across the proteome. *Nat Chem* 2021;13:651–9.
- [54] Klein BJ, et al. Structural insights into the π - π - π stacking mechanism and DNA-binding activity of the YEATS domain. *Nat Commun* 2018;9:4574.
- [55] Chen PY, Aman H, Can M, Ragsdale SW, Drennan CL. Binding site for coenzyme A revealed in the structure of pyruvate:ferredoxin oxidoreductase from *Moorella thermoacetica*. *Proc Natl Acad Sci USA* 2018;115:3846–51.
- [56] Boehr DD, Farley AR, Wright GD, Cox JR. Analysis of the π - π stacking interactions between the aminoglycoside antibiotic kinase APH(3')-IIIa and its nucleotide ligands. *Chem Biol* 2002;9:1209–17.
- [57] Gallivan JP, Dougherty DA. Cation- π interactions in structural biology. *Proc Natl Acad Sci USA* 1999;96:9459–64.
- [58] Zanatta G, et al. Valproic acid interactions with the NavMs voltage-gated sodium channel. *Proc Natl Acad Sci USA* 2019. <https://doi.org/10.1073/pnas.1909696116>
- [59] Chothia C, Janin J. Principles of protein-protein recognition. *Nature* 1975;256:705–8.
- [60] Onufriev AV, Case DA. Generalized Born implicit solvent models for biomolecules. *Annu Rev Biophys* 2019;48:275–96.
- [61] Case DA, et al. The Amber biomolecular simulation programs. *J Comput Chem* 2005;26:1668–88.
- [62] Wang J, et al. Computational insights into the membrane fusion mechanism of SARS-CoV-2 at the cellular level. *Comput Struct Biotechnol J* 2021;19:5019–28.